Analysis of two-color laser-induced electron emission from a biased metal surface using an exact quantum mechanical solution

Yi Luo and Peng Zhang[*]

Department of Electrical and Computer Engineering, Michigan State University, East Lansing, Michigan 48824-1226, USA

Photoelectron emission from solids, as driven by high-intensity lasers, offers a platform for the coherent control of electron motion on ultrashort spatiotemporal scales. By solving the time-dependent Schrödinger equation, we present an exact analytical solution for the nonlinear ultrafast electron emission from a dc-biased metal surface illuminated by two-color laser fields. We systematically examine the combined effects of a dc electric field and two-color laser fields. In addition to the remarkable tunability of electron emission processes due to interference from two-color laser fields, we find that a strong dc electric field not only opens up more tunneling emission channels, but also introduces intense modulation to the emission current. We find surprising results that strong current modulation (with respect to the phase difference of the two-color lasers) persists ($>70\%$), even with a large dc bias (i.e., ratio of the electric fields for dc : fundamental laser : second-harmonic laser $\cong 1 : 0.5 : 0.07$). In the meantime, the average emission current level increases by about three orders of magnitude relative to the case of zero dc bias. Application of our model to time-resolved photoelectron spectroscopy is exemplified and shows that the dynamics of the n-photon excited states depends strongly on the applied dc field. Our study suggests a practical way to maintain a strong modulation to high current photoemission, by the addition of a large dc bias for two-color laser-induced electron emission.

I. INTRODUCTION

Photoelectron emission from nanotips with strong-field lasers is a powerful technique for controlling ultrafast electron dynamics [1–11], which makes it important in many research areas, including time-resolved electron microscopy [12–15], free-electron lasers [16,17], carrier-envelope-phase detection [18–20], and nanoscale vacuum electronics [21–25]. In the last decade, the underlying emission mechanisms have been broadly studied [1–11,18,20,26–30]. Hommelhoff *et al.* [1,18] reported coherent electron emission from a metal nanotip driven by a low-power femtosecond laser. Bormann *et al.* [4] and Schenk *et al.* [5] demonstrated the transition from multiphoton emission to optical-field emission regimes under a strong-field laser. Yanagisawa *et al.* [26,27] studied the photoemission field distribution on a tungsten tip with different azimuthal and polar orientations. Yalunin *et al.* [28] presented a comprehensive theoretical treatment for photoemission from metal surfaces, including perturbation theory, the Floquet method, and the Crank-Nicolson numerical approach. Zhang and Lau [30] developed an exact theory for photoelectron emission due to the combination of a dc electric field and

a single-frequency laser field. Piglosiewicz *et al.* [20] explored the carrier-envelope-phase effects on the strong-field photoemission from a gold nanotip.

Recently, there has been strong interest in photoelectron emission from nanostructures, as driven by two-color lasers [9–11,29,31], because of the relatively straightforward implementation of strong-field waveform control of the two-color lasers and of the resulting substantial emission current modulation. In particular, Förster *et al.* [9] experimentally demonstrated great flexibility in the coherent control of two-color photoemission from a tungsten nanotip by the interference effect. Most recently, we developed an exact quantum mechanical model for two-color photoemission [29], showing excellent agreement with the experimental results reported in Ref. [9] on the current modulation depth. Previous studies testify [18,30] that a strong dc field can dramatically change the photoemission characteristics and modulate both the emission current and photoelectron energy distribution. It is thus interesting and important to investigate the role of dc bias on two-color photoemission, which is expected to introduce more flexibility into electron emission due to the nonlinear interplay of the dc field and the two-color laser fields.

Here, we present an analytical model for nonlinear ultrafast electron emission from a dc-biased metal surface, as driven by two-color laser fields, by solving the

_____
[*]pz@egr.msu.edu

time-dependent Schrödinger equation exactly. The model accounts for various emission processes, including multiphoton emission, photoinduced over-barrier emission, direct tunneling emission, or field emission, in a single formulation. We provide a comprehensive analysis of the electron emission properties under various combinations of laser intensities and frequencies, dc fields, and relative phase differences of the two lasers. We study the effects of image charge on the emission current, which allows an examination of the sensitivity of photoemission to the shape of potential barrier. The application of our analytical model to the time-resolved photoelectron spectroscopy of one-dimensional (1D) systems is also demonstrated. We should emphasize that our model is 1D, which may be readily applied to the study of the photoemission process from 1D structures, such as nanoscopic tips.

II. ANALYTICAL SOLUTION

In our ID model (see Fig. 1), electrons with an initial energy ε are emitted from a dc-biased metal surface at $x = 0$; F_0 is the dc electric field; the two-color laser fields are $F_1\cos(\omega t)$ and $F_2\cos(\beta\omega t + \theta)$, where F_1 and F_2 are the amplitudes of laser fields, ω is the fundamental laser frequency, β is a positive integer, and θ is the phase difference between the two-color lasers. The electric fields of the lasers are assumed to be perpendicular to the flat metal surface. For simplicity, the scattering effect of photoexcited electrons with phonons and other electrons in the laser penetration depth are not included in our model [29,30]. Therefore, a time-varying potential barrier will exist across the metal-vacuum interface,

$$\Phi(x,\ t) = \begin{cases} 0, & x < 0 \\ V_0 - eF_0 x - eF_1 x \cos(\omega t) - eF_2 x \cos(\beta\omega t + \theta), & x \geq 0, \end{cases} \tag{1}$$

where $V_0 = E_F + W$; E_F and W are the Fermi energy and work function of the metal, respectively, and e is the elementary charge.

The electron wave function $\psi(x,\ t)$ is obtained by solving the time-dependent Schrödinger equation,

$$i\hbar\frac{\partial\psi(x,\ t)}{\partial t} = -\frac{\hbar^2}{2m}\frac{\partial^2\psi(x,\ t)}{\partial x^2} + \Phi(x,\ t)\psi(x,\ t), \tag{2}$$

where $\hbar$ is the reduced Plank constant, m is the electron mass, and $\Phi(x,\ t)$ is the potential energy given in Eq. (1).

An exact solution to Eq. (2) for $x \geq 0$ is found to be (see Appendix for the method),

$$\psi(x,\ t) = \sum_{n=-\infty}^{\infty} T_n[\mathrm{Ai}(-\eta_n) - i\mathrm{Bi}(-\eta_n)]$$
$$\times \exp\left(-i\frac{\varepsilon}{\hbar}t - in\omega t\right)$$
$$\times \exp\left(\frac{ie}{\hbar}Lx + \frac{ie^2}{8\hbar m}M - \frac{ie^2 F_1 F_2}{2\beta\hbar m\omega^2}N\right.$$
$$\left. - \frac{ie^2 F_0}{\hbar m}Q\right), \quad x \geq 0, \tag{3}$$

where $L = [F_1\sin(\omega t)/\omega] + [F_2\sin(\beta\omega t + \theta)/\beta\omega]$; $M = [F_1^2\sin(2\omega t)/\omega^3] + [F_2^2\sin(2\beta\omega t + 2\theta)/\beta^3\omega^3]$; $N = \{\sin[(\beta - 1)\omega t + \theta]/(\beta - 1)\omega\} - \{\sin[(\beta + 1)\omega t + \theta]/(\beta + 1)\omega\}$; $Q = [F_1\sin(\omega t)/\omega^3] + [F_2\sin(\beta\omega t + \theta)/\beta^3\omega^3]$; $\eta_n = \{(E_n/eF_0) + x + [eF_1\cos(\omega t)/m\omega^2] + [eF_2\cos(\beta\omega t + \theta)/m\beta^2\omega^2]\}(2emF_0/\hbar^2)^{1/3}$; the drift kinetic energy is

$E_n = \varepsilon + n\hbar\omega - E_F - W - U_{p1} - U_{p2}$; the ponderomotive energies are $U_{p1} = e^2 F_1^2/4m\omega^2$ and $U_{p2} = e^2 F_2^2/4m\beta^2\omega^2$; Ai and Bi are the Airy functions of the first and
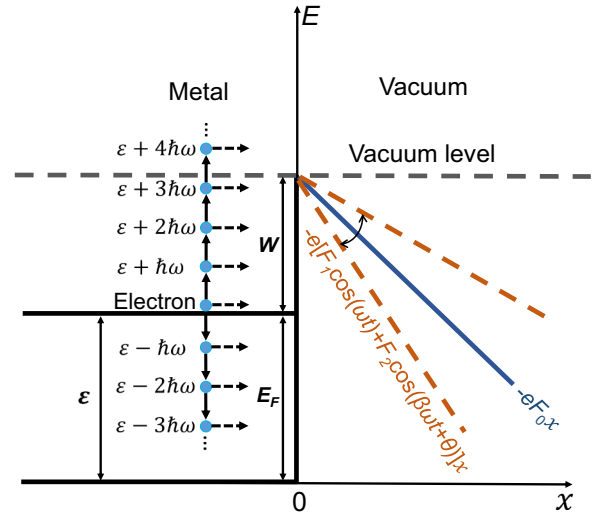

FIG. 1. Energy diagram for photoemission under two-color laser fields and a dc bias. Electrons with initial energy ε are emitted from the dc-biased metal-vacuum interface at $x = 0$, with a transmitted energy of $\varepsilon + n\hbar\omega$, due to the n-photon contribution [multiphoton absorption ($n > 0$), tunneling ($n = 0$), and multiphoton emission ($n < 0$)], where n is an integer. The fundamental and harmonic laser fields are $F_1\cos(\omega t)$ and $F_2\cos(\beta\omega t + \theta)$, respectively. The dc electric field is F_0. The photon energy of the fundamental (harmonic) laser is $\hbar\omega$ ($\beta\hbar\omega$). E_F and W are the Fermi energy and work function of the metal, respectively.

second kind, respectively, showing an outgoing wave traveling in the $+x$ direction (see Fig. 1) [30,32,33]; T_n represents the transmission coefficient; and ε is the initial energy of the electron. It is easy to find that Eq. (3) is periodic with a time period of $2\pi/\omega$; therefore, Eq. (3) is ready to be recast into a Fourier series, which denotes the superposition of transmitted traveling electron waves with energies $\varepsilon + n\hbar\omega$. These ladder eigenenergies are made possible by multiphoton absorption ($n > 0$), tunneling ($n = 0$), and multiphoton emission ($n < 0$) [28–30].

The solution to Eq. (2) for $x < 0$ is,

$$
\psi(x,\,t) = \exp\left(-\frac{i\varepsilon t}{\hbar} + ik_0 x\right)
$$
$$
+ \sum_{n=-\infty}^{\infty} R_n \exp\left(-i\frac{\varepsilon + n\hbar\omega}{\hbar}t - ik_n x\right),\ x < 0,
$$
(4)

which denotes the superposition of an incident plane wave and a set of reflected waves with reflection coefficient R_n and energies $\varepsilon + n\hbar\omega$, where $k_0 = \sqrt{2m\varepsilon/\hbar^2}$ and $k_n = \sqrt{2m(\varepsilon + n\hbar\omega)/\hbar^2}$.

Applying the boundary conditions that both $\psi(x, t)$ and $\partial\psi(x, t)/\partial x$ are continuous at $x = 0$, Fourier transform yields, in nondimensional quantities [29,30], $\bar{\varepsilon} = \varepsilon/W$, $\bar{\omega} = \omega\hbar/W$, $\bar{t} = tW/\hbar$, $\bar{E}_F = E_F/W$, $\bar{x} = x/\lambda_0$, $\lambda_0 = \sqrt{\hbar^2/2mW}$, $\bar{F}_0 = F_0 e\lambda_0/W$, $\bar{F}_1 = F_1 e\lambda_0/W$, $\bar{F}_2 = F_2 e\lambda_0/W$, $\bar{U}_{p1} = U_{p1}/W$, $\bar{U}_{p2} = U_{p2}/W$, the following equations,

$$
2\sqrt{\bar{\varepsilon}}\delta(l) = \sum_{n=-\infty}^{\infty} T_n\left[\sqrt{\bar{\varepsilon} + l\bar{\omega}}P_{n(n-l)} + Q_{n(n-l)}\right],\quad (5)
$$

where $\delta(l)$, $P_{n(n-l)}$, and $Q_{n(n-l)}$ are given by,

$$
\delta(l) = \begin{cases} 1, & l = 0, \\ 0, & l \neq 0, \end{cases} \quad (6a)
$$

$$
P_{nl} = \frac{1}{2\pi}\int_0^{2\pi} p_n(\bar{\omega}\bar{t})e^{-il\bar{\omega}\bar{t}}d(\bar{\omega}\bar{t}),
$$

$$
Q_{nl} = \frac{1}{2\pi}\int_0^{2\pi} q_n(\bar{\omega}\bar{t})e^{-il\bar{\omega}\bar{t}}d(\bar{\omega}\bar{t}), \quad (6b)
$$

$$
p_n(\bar{\omega}\bar{t}) = \phi(\bar{\omega}\bar{t})[\mathrm{Ai}(\alpha_n) - i\mathrm{Bi}(\alpha_n)], \quad (6c)
$$

$$
q_n(\bar{\omega}\bar{t}) = \phi(\bar{\omega}\bar{t})z_n(\bar{\omega}\bar{t}), \quad (6d)
$$

$$
\phi(\bar{\omega}\bar{t}) = e^{i\bar{M} - (i\bar{F}_1\bar{F}_2/\beta\bar{\omega}^2)\bar{N}} \times e^{-i2\bar{F}_0\bar{Q}}, \quad (6e)
$$

$$
z_n(\bar{\omega}\bar{t}) = \bar{L}[\mathrm{Ai}(\alpha_n) - i\mathrm{Bi}(\alpha_n)] + \bar{F}_0^{1/3}[i\mathrm{Ai}'(\alpha_n) + \mathrm{Bi}'(\alpha_n)],
$$
(6f)

with $\bar{L} = (\bar{F}_1/\bar{\omega})\sin(\bar{\omega}\bar{t}) + (\bar{F}_2/\beta\bar{\omega})\sin(\beta\bar{\omega}\bar{t} + \theta)$, $\bar{M} = [\bar{F}_1^2\sin(2\bar{\omega}\bar{t})/4\bar{\omega}^3] + [\bar{F}_2^2\sin(2\beta\bar{\omega}\bar{t} + 2\theta)/4\beta^3\bar{\omega}^3]$, $\bar{N} = \{\sin[(\beta - 1)\bar{\omega}\bar{t} + \theta]/(\beta - 1)\bar{\omega}\} - \{\sin[(\beta + 1)\bar{\omega}\bar{t} + \theta]/(\beta + 1)\bar{\omega}\}$, $\bar{Q} = (\bar{F}_1/\bar{\omega}^3)\sin(\bar{\omega}\bar{t}) + (\bar{F}_2/\beta^3\bar{\omega}^3)\sin(\beta\bar{\omega}\bar{t} + \theta)$, $\alpha_n = -\bar{F}_0^{1/3}[(\bar{E}_n/\bar{F}_0) + (2\bar{F}_1/\bar{\omega}^2)\cos(\bar{\omega}\bar{t}) + (2\bar{F}_2/\beta^2\bar{\omega}^2)\cos(\beta\bar{\omega}\bar{t} + \theta)]$, and $\bar{E}_n = \bar{\varepsilon} + n\bar{\omega} - \bar{E}_F - \bar{U}_{p1} - \bar{U}_{p2} - 1$. Since Eq. (5) is derived from the conditions that electron wave function and its first derivative are continuous at the metal-vacuum interface ($x = 0$), $p_n(\bar{\omega}\bar{t})$ and $q_n(\bar{\omega}\bar{t})$ in Eqs. (6c) and (6d) represent the phase factor of the nth-state wave function and of its spatial derivative at $\bar{x} = 0$, respectively. P_{nl} and Q_{nl} are the lth Fourier coefficients of p_n and q_n respectively. The transmission coefficient T_n (and therefore, the reflection coefficient R_n) is calculated from Eq. (5).

The normalized emission current density is defined as the ratio of the transmitted probability current density over the incident probability current density, $w(\varepsilon, x, t) = J_t(\varepsilon, x, t)/J_i(\varepsilon, x, t)$, where the probability current density is $J(x, t) = (i\hbar/2m)(\psi\partial\psi^*/\partial x - \psi^*\partial\psi/\partial x) = (i\hbar/2m)\sum_{n=-\infty}^{\infty}\sum_{l=-\infty}^{\infty}(\psi_n\partial\psi_l^*/\partial x - \psi_n^*\partial\psi_l/\partial x)$. Thus, the normalized instantaneous emission current density is,

$$
w(\bar{\varepsilon}, \bar{x}, \bar{t}) = \frac{1}{\sqrt{\bar{\varepsilon}}}\sum_{n=-\infty}^{\infty}\sum_{l=-\infty}^{\infty}\mathrm{Im}[e^{i(l-n)\bar{\omega}\bar{t}}T_n T_l^*(C + iD)],
$$
(7a)

$$
C = \bar{L}[\mathrm{Ai}(-\overline{\eta_l})\mathrm{Bi}(-\overline{\eta_n}) - \mathrm{Ai}(-\overline{\eta_n})\mathrm{Bi}(-\overline{\eta_l})]
$$
$$
+ \bar{F}_0^{1/3}[\mathrm{Ai}(-\overline{\eta_n})\mathrm{Ai}'(-\overline{\eta_l}) + \mathrm{Bi}(-\overline{\eta_n})\mathrm{Bi}'(-\overline{\eta_l})], \quad (7b)
$$

$$
D = \bar{L}[\mathrm{Ai}(-\overline{\eta_l})\mathrm{Ai}(-\overline{\eta_n}) + \mathrm{Bi}(-\overline{\eta_l})\mathrm{Bi}(-\overline{\eta_n})]
$$
$$
+ \bar{F}_0^{1/3}[\mathrm{Ai}(-\overline{\eta_n})\mathrm{Bi}'(-\overline{\eta_l}) - \mathrm{Bi}(-\overline{\eta_n})\mathrm{Ai}'(-\overline{\eta_l})], \quad (7c)
$$

where $\overline{\eta_n} = \bar{F}_0^{1/3}[(\bar{E}_n/\bar{F}_0) + (2\bar{F}_1/\bar{\omega}^2)\cos(\bar{\omega}\bar{t}) + (2\bar{F}_2/\beta^2\bar{\omega}^2)\cos(\beta\bar{\omega}\bar{t} + \theta) + \bar{x}]$, and $\bar{L}$ is defined in Eq. (6f). The normalized time-averaged emission current density is obtained as,

$$
\langle w(\bar{\varepsilon})\rangle = \sum_{n=-\infty}^{\infty}\langle w_n(\bar{\varepsilon})\rangle, \quad \langle w_n(\bar{\varepsilon})\rangle = |T_n|^2\frac{\bar{F}_0^{1/3}}{\pi\sqrt{\bar{\varepsilon}}}, \quad (8)
$$

where $\langle w_n(\bar{\varepsilon})\rangle$ denotes the time-averaged emission current density through the nth channel, with emitted electron energy $\varepsilon + n\hbar\omega$ due to the n-photon contribution [30]. Notably, this 1D analytical model assumes no variation in the direction perpendicular to the electric field, which may

be realized when the extension of the target in the laser propagation direction is smaller than the wavelength of the light field, e.g., a nanotip.

III. RESULTS AND DISCUSSION

First, to understand the detailed underlying multiphoton emission processes, the photoelectron energy spectra for different combinations of in-phase ($\theta = 0$) two-color laser fields, F_1 (at frequency ω) and F_2 (at frequency 2ω), and dc fields, F_0, are shown in Fig. 2. The results are calculated from Eq. (8), except for the $F_0 = 0$ cases [Figs. 2(a) and 2(d)], which are obtained from our previous work [29]. The wavelength of the fundamental laser F_1 is 800 nm ($\hbar\omega = 1.55$ eV). F_2 has a frequency of 2ω [i.e., $\beta = 2$ in Eq. (1)]. The metal is assumed to be gold [4,29,30], with a Fermi energy of $E_F = 5.53$ eV and a work function of $W = 5.1$ eV. Since most of the emission electrons from sources are located near the Fermi level [28,30,33–35], we choose the electron initial energy $\varepsilon = E_F$ for simplicity. Unless stated otherwise, these are the default values for the calculations in this paper.

When the dc field, F_0, is turned off [cf. Figs. 2(a) and 2(d)], the dominant emission process is the four-photon absorption ($n = 4$) for the fundamental laser; this indicates that the electron at the Fermi level needs to absorb at least four photons to overcome the potential barrier W (see Fig. 1). This is consistent with the ratio of the work function over the fundamental laser photon energy, $W/\hbar\omega = 3.29$. Applying a strong dc field, F_0, to the metal is able to open the tunneling emission channels below the over-barrier emission threshold ($n < 4$), as shown in Figs. 2(b), 2(c), 2(e), and 2(f). This is because the dc field could sufficiently narrow the potential barrier at the metal-vacuum interface ($x = 0$) (see Fig. 1), enabling the tunneling emission process for $n < 4$. As F_0 increases from Figs. 2(b) to 2(c), and 2(e) to 2(f), the potential barrier becomes narrower, increasing the probability of electron emission through the tunneling channels, and the emission channel with the highest probability shifts towards the direct tunneling process ($n = 0$), which is consistent with the observation in Ref. [30]. Here, a local dc electric field of up to 8 V/nm is realized in experiments at sharp metallic tips, via either powerful THz pulses, or laboratory-scale setup based on pulsed capacitor discharge [2,36]. For a given dc field, F_0, as either laser field (F_1 or F_2) increases, the energy spectra become broader because more emission channels open up and contribute to photoemission. In the
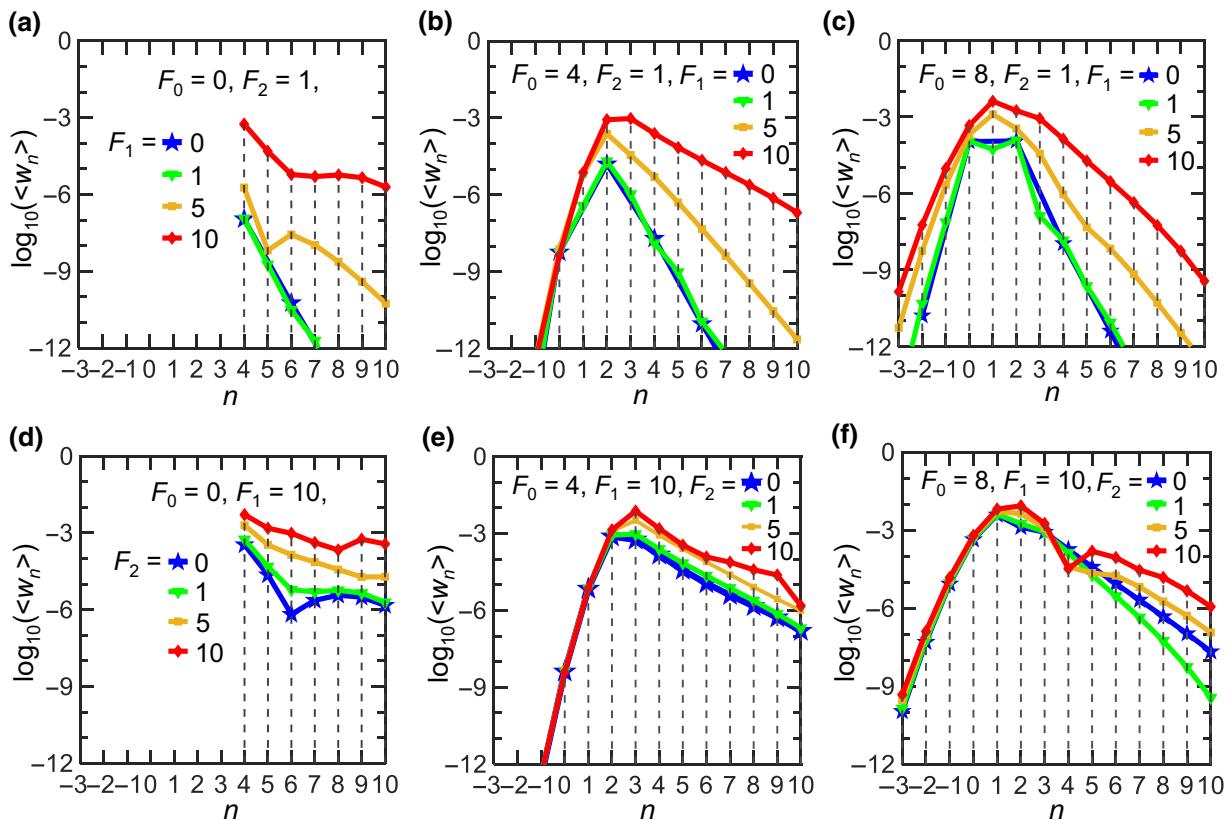

FIG. 2.   Photoelectron energy spectra under different in-phase (i.e., $\theta = 0$) laser fields, F_1 (at frequency ω) and F_2 (at frequency 2ω), and dc fields, F_0. In (a)–(c) F_2 is fixed as 1 V/nm, and in (d)–(f) F_1 is fixed as 10 V/nm. The n-photon process (i.e., the horizontal axis) is given with respect to the fundamental laser frequency, which measures the energy of the emitted electrons. The units of dc field, F_0, and laser fields, F_1 and F_2, are V/nm throughout.

meantime, the dominant emission process shifts to the channel with larger n because electrons have to absorb a sufficient number of photons to overcome the increasing ponderomotive energies $U_{p1} = e^2 F_1^2 / 4m\omega^2$ and $U_{p2} = e^2 F_2^2 / 4m\beta^2\omega^2$ with increasing laser field strength; thus exhibiting the transition from the multiphoton regime to the optical strong-field regime [37]. These observations are consistent with previous experimentally and theoretically obtained energy spectra [5,7,20,29,30]. Since F_2 is fixed at 1 V/nm in Figs. 2(a)–2(c), whereas F_1 is fixed at a larger value of 10 V/nm in Figs. 2(d)–2(f), the spectra in Figs. 2(d)–2(f) are generally broader than those in Figs. 2(a)–2(c).

In general, as the dc field, F_0, or the laser field, F_1 or F_2, increases, the total emission current $\langle w \rangle$ increases because more emission channels are opened up (see Fig. 2). When one field becomes much stronger than the other two, the

total current emission is dominated by this largest field. Figure 3 shows the normalized total time-averaged emission current density $\langle w \rangle$ as a function of the fundamental laser field, F_1, for different second-harmonic laser fields, F_2, and dc fields, F_0, when $\theta = 0$ and π. When the second-harmonic field, F_2, increases, $\langle w \rangle$ becomes less sensitive to F_1, since F_2 gradually dominates the emission process. For single-frequency laser-induced electron emission [30], it is confirmed that, in the multiphoton regime, the slope of the curve of $\langle w \rangle$ versus F_1 follows the scale $\langle w \rangle \propto F_1^{2n}$; this indicates that the dominant emission process is the n-photon process. This scale is not strictly valid for the two-color photoemission here; however, the change of the slope of the curves could still manifest the shift of the main n-photon emission process. For instance, as the dc field, F_0, increases from Figs. 3(a) to 3(c) for $\theta = 0$ and from 3(d) to 3(f) for $\theta = \pi$, the slope of $\langle w \rangle$ for a given F_2
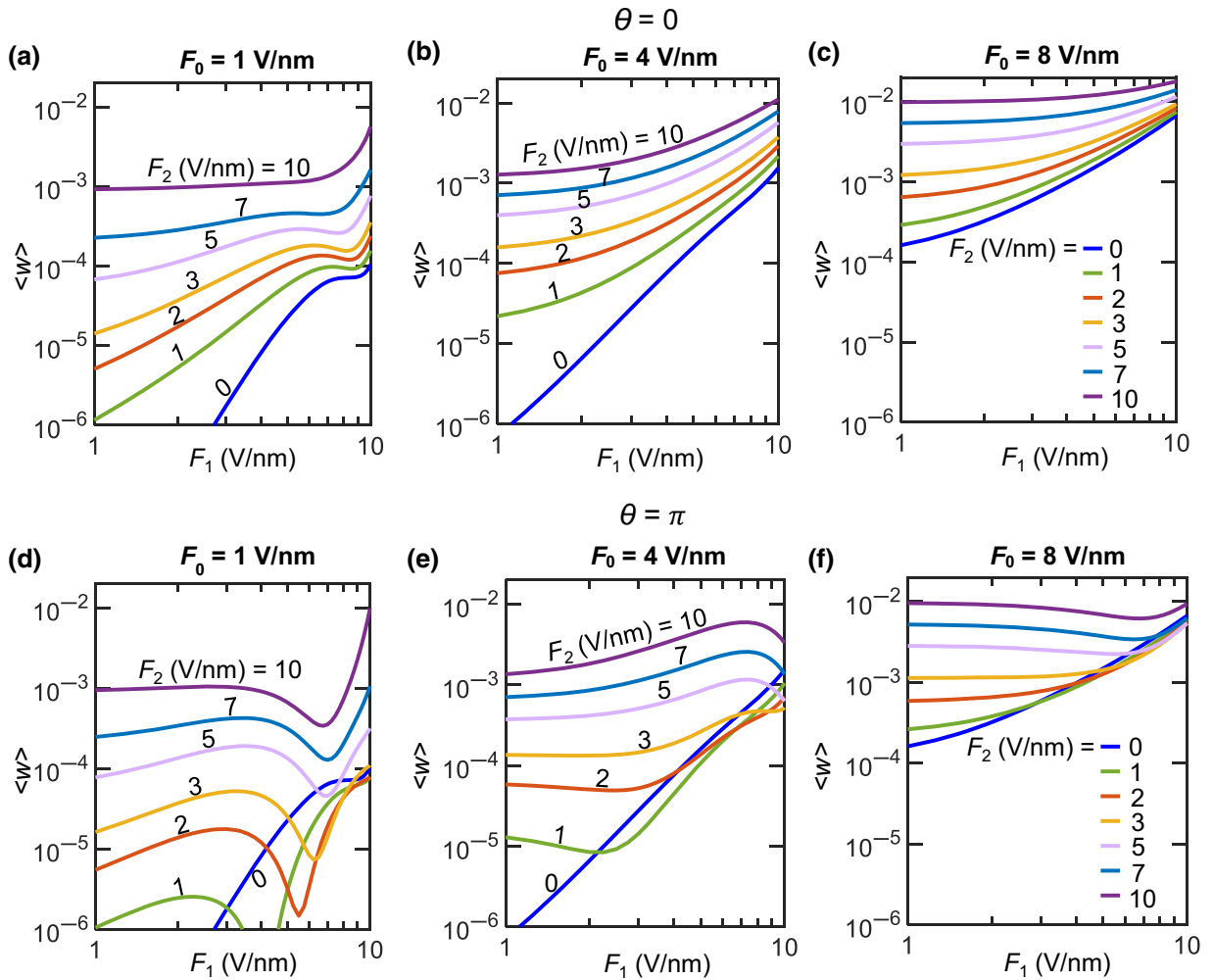

FIG. 3. Normalized total time-averaged emission current density $\langle w \rangle$ for the phase difference between the two-color lasers (a)–(c) $\theta = 0$, and (d)–(f) $\theta = \pi$, as a function of the fundamental laser field, F_1, under various combinations of the second-harmonic laser field, F_2, and dc electric field, F_0. The laser intensity is related to the laser electric field by $I_{1,2}$ (W/cm^2) $= 1.33 \times 10^{11} \times [F_{1,2}$ (V/nm)$]^2$ [29,30].

decreases, since the dominant emission process shifts to lower emission channels.

The above trend is also reflected in Fig. 4, which shows the normalized time-averaged emission current density $\langle w_n \rangle$ through the nth channel as a function of the fundamental laser field, F_1, for fixed $F_2 = 5$ V/nm. For both cases of $\theta = 0$ and $\theta = \pi$, when F_0 increases from 1 to 4 V/nm, the dominant emission channel shifts from $n = 3$ to $n = 2$, in general [cf. Figs. 4(a), 4(b), 4(d), and 4(e)]. When F_0 reaches 8 V/nm, the dominant emission process transits from the two-photon absorption ($n = 2$) for $F_1 \leq 7$ V/nm to single-photon absorption ($n = 1$) for $F_1 > 7$ V/nm [cf. Figs. 4(c) and 4(f)]. It is clear that direct tunneling ($n = 0$) is almost independent of the laser field F_1, but very sensitive to the dc field F_0.

When the phase difference, θ, changes from 0 to π, due to the interference effect between the two lasers, new dips appear in the curves of $\langle w_n \rangle$, which can cause changes to the dominant emission process when F_1 increases. For example, in Fig. 4(e), the dip in the curve of $n = 2$ at around $F_1 = 5.5$ V/nm changes the dominant emission to the $n = 3$ process instead of the $n = 2$ process otherwise observed. The dips are also present in the total emission current $\langle w \rangle$ [cf. Figs. 3(d) and 3(e)], which is consistent with our previous observation of two-color laser-induced emission without a dc bias (see Fig. 3 in Ref. [29]). As the dc field, F_0, becomes larger, these new dips gradually disappear, as shown in Figs. 3(f) and 4(f), because the interference effect of the two lasers is masked by the strong dc field.

The total emission current density $\langle w \rangle$ as a function of the dc field, F_0, for different laser fields, F_1 and F_2, is shown in Fig. 5. When the phase difference of the two lasers $\theta = 0$, the total emission current density $\langle w \rangle$ increases as either of the laser fields (F_1 or F_2) increases. When the dc field F_0 becomes larger, $\langle w \rangle$ becomes less sensitive to the laser fields, since the Fowler-Nordheim-like field emission [32] due to the dc electric field becomes more important than the over-barrier photoemission. The curves in Fig. 5(a) resemble the experimentally measured trends of the voltage- and power-dependent electron flux (cf. Fig. 2 in Ref. [2]). As shown in Figs. 5(d)–5(f), when $\theta = \pi$, due to the interference effect of the two lasers, the curves are intertwined, indicating strong nonlinear dependence of the emission current on the laser fields. For large F_0 (≥ 7 V/nm) and small F_2 ($= 1$ V/nm) in Fig. 5(d), $\langle w \rangle$ remains almost the same as that with $\theta = 0$ in Fig. 5(a), since the interference effect is suppressed by the dc field.
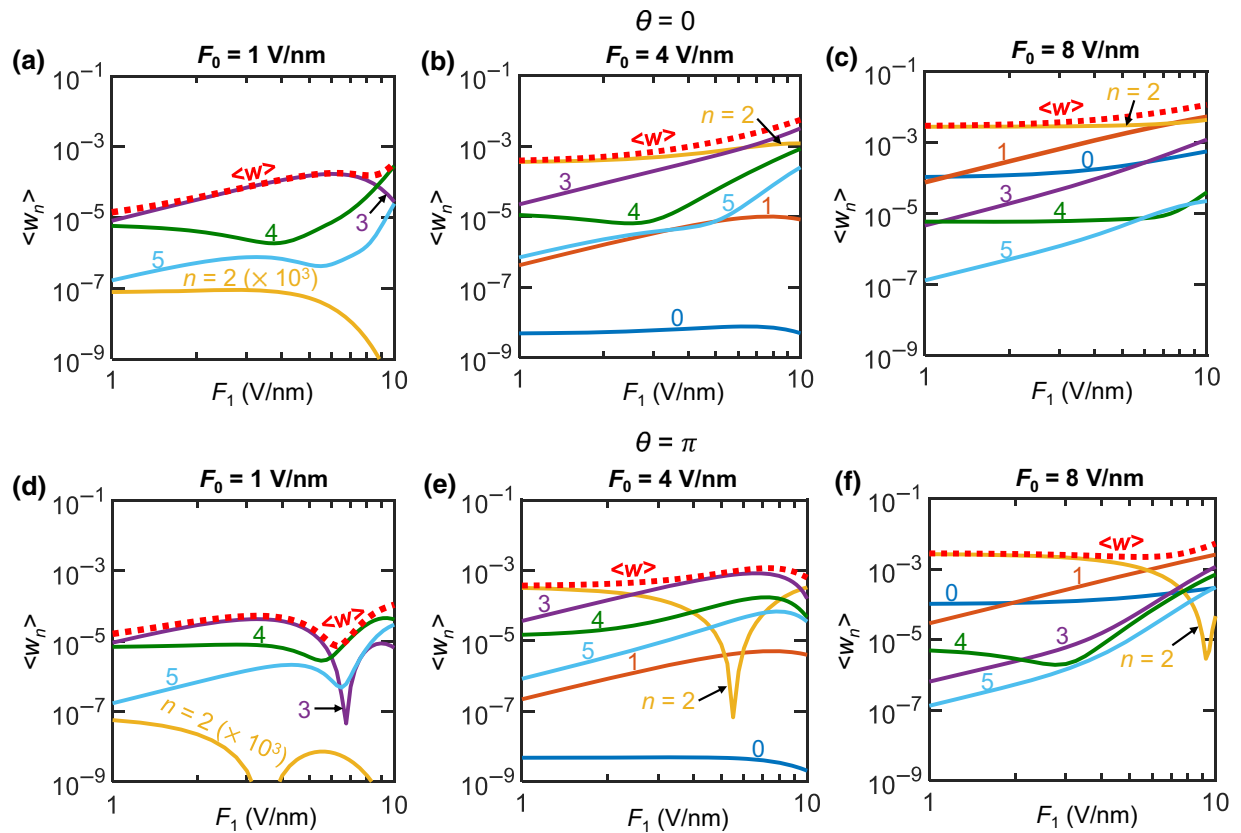

FIG. 4. Normalized time-averaged emission current density $\langle w_n \rangle$ through the nth channel for the phase difference between the two-color lasers (a)–(c), $\theta = 0$, and (d)–(f) $\theta = \pi$, as a function of the fundamental laser field, F_1, for various dc electric fields, F_0, when the second-harmonic laser field is $F_2 = 5$ V/nm. Dotted lines represent the normalized total emission current $\langle w \rangle = \sum_n w_n$.
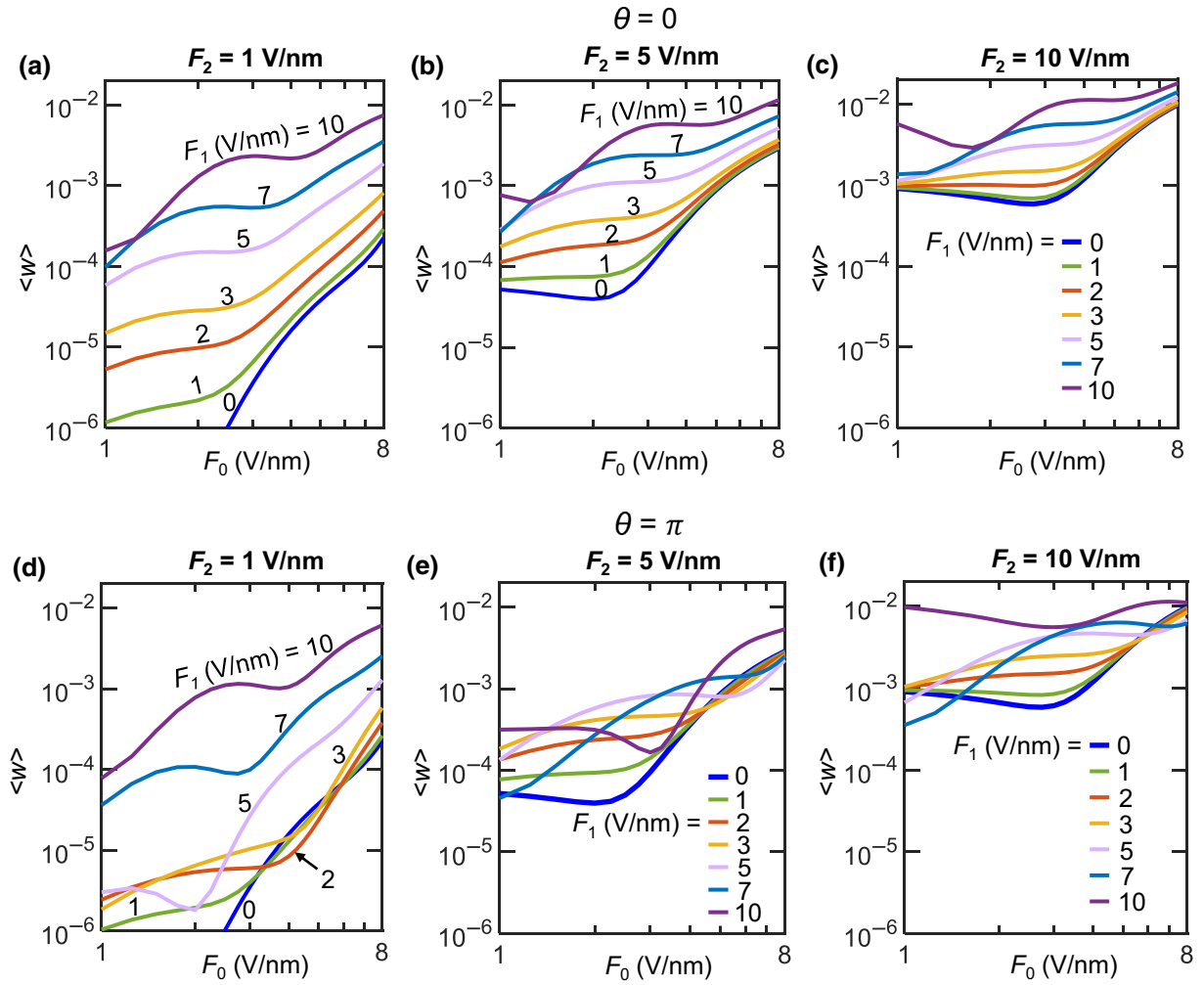
FIG. 5.   Normalized total time-averaged emission current density $\langle w \rangle$ for the phase difference between the two-color lasers (a)–(c), $\theta = 0$, and (d)–(f) $\theta = \pi$, as a function of the dc electric field, F_0, for different fundamental laser fields, F_1, and second-harmonic laser fields, F_2. Intertwined curves in (d)–(f) indicate the strong interference effect of the two lasers.

Figure 6 shows the emission current density $\langle w_n \rangle$ as a function of the dc field F_0 for the case of $F_1 = 7$ V/nm. It is clear that the dominant multiphoton emission process shifts to smaller n as F_0 increases. As F_2 increases, these shifts would occur at larger dc field F_0. For example, when $\theta = 0$, the shifts of three-photon emission to two-photon emission occur at $F_0 \approx 3.5$, 4, and 4.5 V/nm when $F_2 = 1$, 5, and 10 V/nm in Figs. 6(a)–6(c), respectively. The shifts of the dominant emission process also depend strongly on the phase difference, θ. For $F_2 = 5$ V/nm, a new dip appears in the curve of $n = 2$ when $\theta = \pi$, compared with the case of $\theta = 0$, leading to the change of the dominant emission channel [i.e., two-photon process in Fig. 6(b) vs single-photon process in Fig. 6(e) at $F_0 \approx 7.5$ V/nm].

Previous studies [9,29] show that changing the phase delay of the two-color lasers is able to modulate the photoemission current, due to the interference effect. By applying a strong dc bias in addition to a weak single

laser field, strong time-varying current emission perseveres and sometimes can even be enhanced [30]. Figure 7 displays the combined effects of the dc field and the interference between two-color lasers on the energy spectra and total emission current; this reveals the strong effects of the dc bias on the photoemission current modulation depth. Figure 7(a) shows the effects of the phase difference, θ, of the two-color lasers on the total emission current density $\langle w \rangle$, under different dc fields, F_0. Here, the ω-laser field, F_1, and the 2ω-laser field, F_2, are fixed as 1.6 and 0.22 V/nm, respectively (i.e., intensity ratio of 2%). It is clear that $\langle w \rangle$ oscillates as a function of θ with a period of 2π, which shows a close resemblance to the experimental observation [see Fig. 2(b) in Ref. [9]]. As the dc field F_0 increases, $\langle w \rangle$ also increases. The maximum (minimum) values of $\langle w \rangle$ occur at around $\theta = 0$ ($\theta = \pi$), when the two-color lasers are in phase (180° out of phase). Figure 7(b) shows the photoelectron
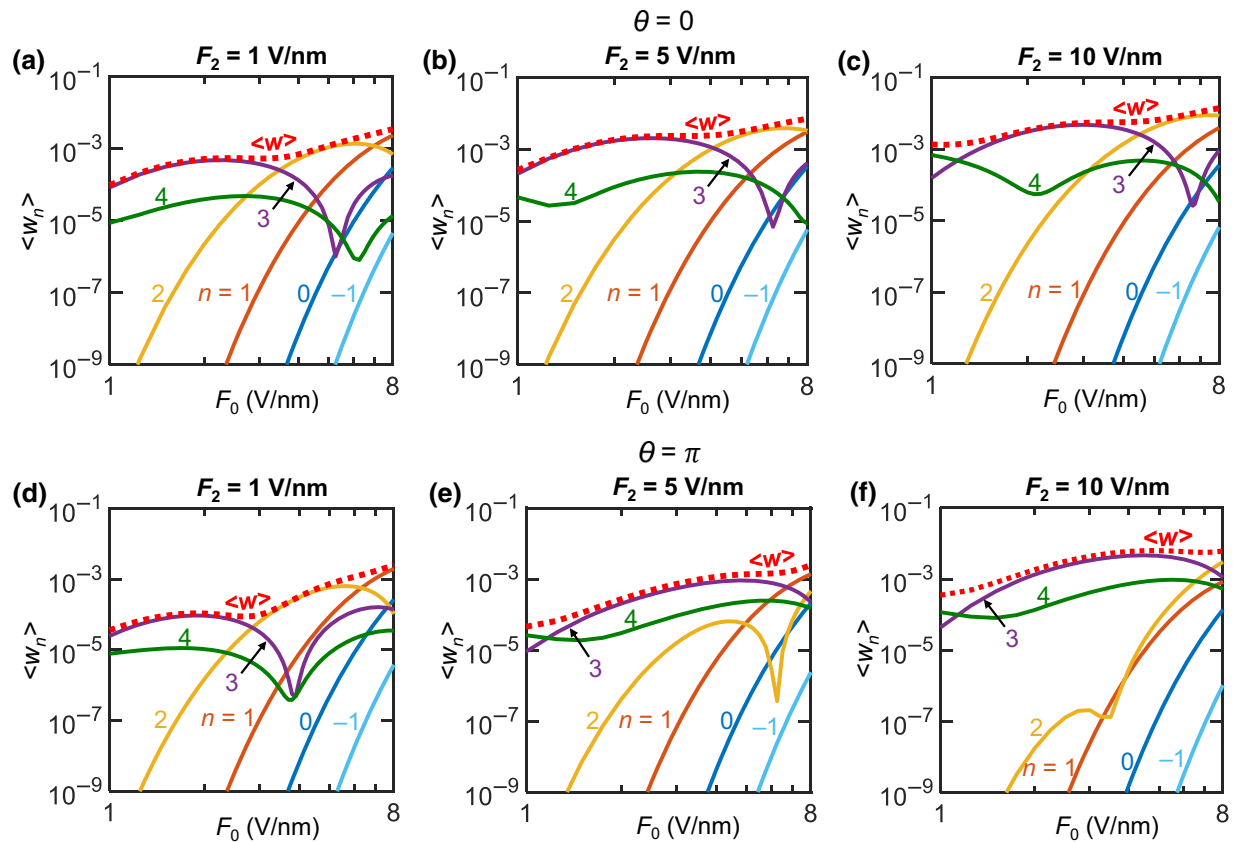
FIG. 6.   Normalized time-averaged emission current density $\langle w_n \rangle$ through the nth channel for the phase difference (a)–(c) $\theta = 0$, and (d)–(f) $\theta = \pi$, as a function of the dc electric field, F_0, for various second-harmonic laser fields, F_2, when the fundamental laser field is $F_1 = 7$ V/nm. Dotted lines represent the normalized total emission current $w = \sum_n \langle w_n \rangle$.

energy spectra of $\langle w \rangle$ at different θ in a single period for the case of $F_0 = 1$ V/nm in Fig. 7(a). When $\theta = 0$ (A), $\pi/2$ (B), and $3\pi/2$ (D), the electron emission probability through the dominant channel ($n = 3$) driven by two-color lasers is larger than that driven by the strong fundamental laser field F_1 alone. However, when $\theta = \pi$ (C), the emission through $n = 3$ driven by the two-color lasers becomes smaller than that driven by F_1 alone, due to the strong interference effect. The emission current driven by the two-color lasers is always larger than that driven by the weak second-harmonic laser field F_2 alone, regardless of θ. These observations are in excellent agreement with the experimentally measured electron spectra (see Fig. 3 in Ref. [9]).

Figure 7(c) summarizes the modulation depth in Fig. 7(a), defined as $\Gamma = (\langle w \rangle_{max} - \langle w \rangle_{min})/(\langle w \rangle_{max} + \langle w \rangle_{min})$, as a function of the dc field, F_0. When F_0 is zero, the modulation depth, Γ, is as high as 99% [29]. As F_0 increases, Γ decreases because the interference effect is gradually suppressed by F_0. When $F_0 = 8$ V/nm, Γ drops to approximately 2.98%; thus showing a strong dependence of current modulation on the dc bias. It is important to note that, even when the dc bias F_0 reaches

3 V/nm (significantly larger than the laser fields $F_1 = 1.6$ and $F_2 = 0.22$ V/nm, corresponding to a ratio of $F_0 : F_1 : F_2 \cong 1 : 0.5 : 0.07$), a current modulation of $\Gamma \geq 70\%$ can still be achieved. This suggests a practical way to maintain a strong current modulation, while increasing the total emission current by orders of magnitude, by simply adding a strong dc bias for two-color laser-induced electron emission.

Since photoelectron emission paths (or channels) depend strongly on the incident laser frequencies, as well as the interferences between them, superimposing different orders of harmonic lasers on the fundamental laser can lead to different photoemission currents. Figure 8 shows the effects of the harmonic order, β, on the total emission current density, $\langle w \rangle$, induced by the two-color lasers of frequency ω and $\beta\omega$ under various dc fields. When the dc field $F_0 = 0$, the maximum value of $\langle w \rangle$ occurs when $\beta = 4$; this is because the maximum emission current happens when the single-photon energy (of the fourth-harmonic laser in this case) roughly equals the potential barrier ($4\hbar\omega/W \approx 1$) [29,30]. By comparing Fig. 8 with Fig. 2, the harmonic order β where the maximum emission current occurs coincides with channel number n of the
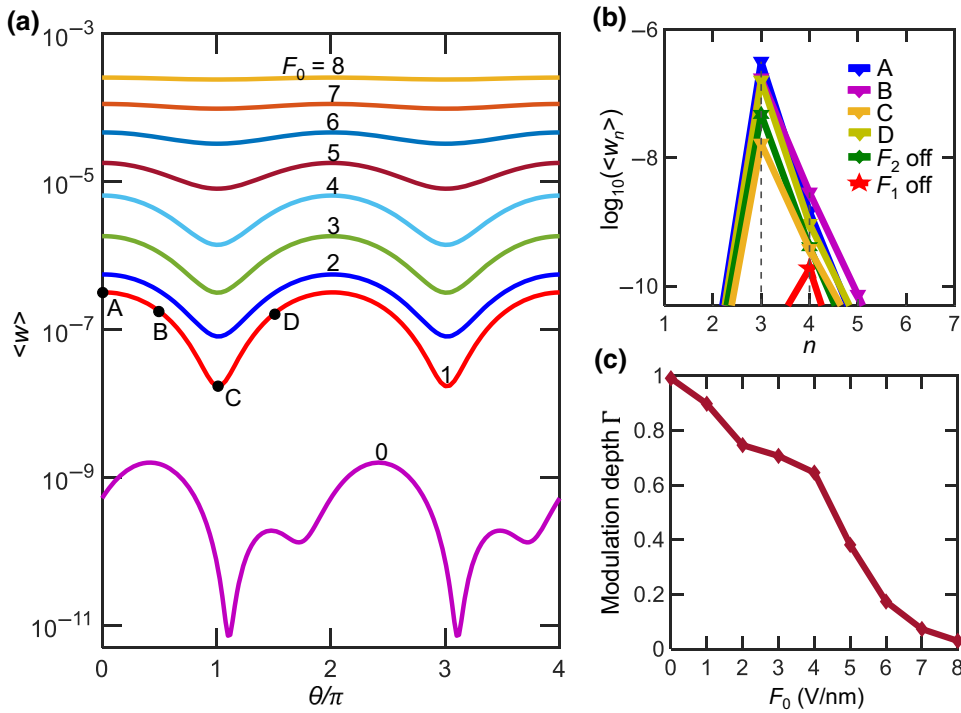
FIG. 7. Emission current modulation depth. (a) Normalized total time-averaged emission current density $\langle w \rangle$ as a function of the phase difference, θ, for different dc electric fields, F_0, with ω-laser field F_1 and 2ω-laser field F_2 fixed at 1.6 and 0.22 V/nm, respectively (experimental laser parameters in Ref. [9]). (b) Energy spectra of the emission current at different values of θ for the case of $F_0 = 1$ V/nm in (a). A, B, C, and D denote $\theta = 0$, $\pi/2$, π, and $3\pi/2$ in (a), respectively. (c) Current modulation depth Γ in (a) as a function of the dc field, F_0. The unit of dc field, F_0, is V/nm throughout.

dominant n-photon process (with respect to the fundamental frequency ω), for a given combination of F_0, F_1, and F_2. As observed in Fig. 8, as F_0 increases, the value of β for the maximum $\langle w \rangle$ shifts to a smaller number. This is consistent with the observation in Fig. 2 that a larger dc field, F_0, changes the dominant n-photon process to a smaller n. When $F_0 \geq 7$ V/nm, the electron emission becomes almost independent of the frequency ($\beta\omega$) of the harmonic laser, since the Fowler-Nordheim-like field emission dominates the emission process. When θ changes from zero to π, for small $F_0 (\leq 4$ V/nm$)$ and $\beta (\leq 4)$, the emission current density $\langle w \rangle$ has a distinct reduction due to the interference effect of the two lasers. However, for large $F_0 (\geq 7$ V/nm$)$, the emission current $\langle w \rangle$ is almost independent of θ for all harmonic orders of the second laser.

Our calculations so far are based on the sharp triangular potential profile (see Fig. 1), which does not include the image-charge effects. Our earlier work [30] demonstrates that the effects of image-charge-induced Schottky barrier lowering on photoemission can be accurately approximated in our model, by simply replacing the work function, W, in Eq. (1) with the effective work function $W_{\text{eff}} = W - 2\sqrt{e^3 F_0 / 16\pi\varepsilon_0}$, where ε_0 is the free space permittivity.

Reduction of the effective surface barrier due to the image-charge effect (or Schottky effect) is another profound effect of dc bias. A comparison between the total emission current density $\langle w \rangle$ with and without the image-charge-induced barrier lowering is shown in Fig. 9. Due to the reduction of potential barrier ($W_{\text{eff}} < W$), the
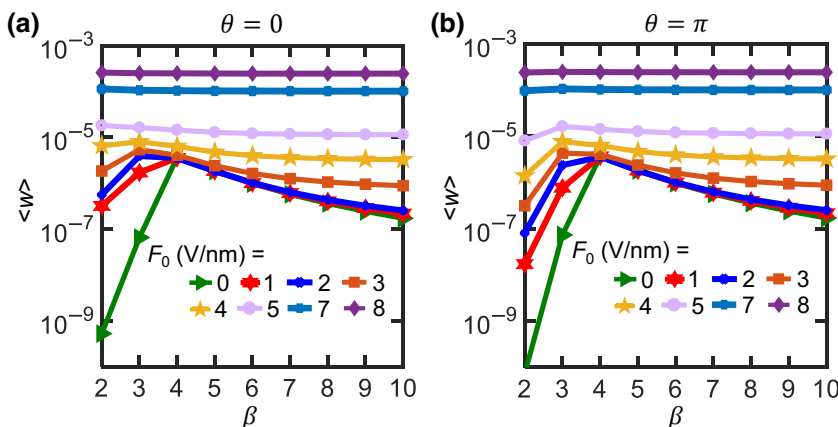

FIG. 8. Normalized total time-averaged emission current density $\langle w \rangle$ as a function of harmonic order β, for the phase difference (a) $\theta = 0$, and (b) $\theta = \pi$. The fundamental ω-laser field $F_1 = 1.6$ V/nm and the harmonic $\beta\omega$-laser field $F_2 = 0.22$ V/nm.
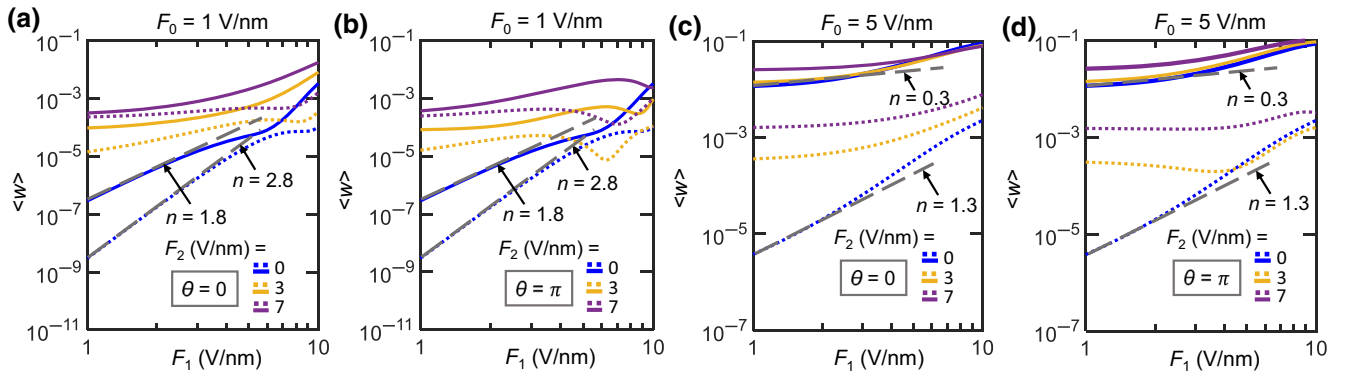
FIG. 9.   Effects of the image-charge-induced barrier lowering on the total emission current $\langle w \rangle$ for various F_0, F_1, F_2, and θ. The solid (dotted) lines represent the cases with (without) the image-charge effect, calculated using the effective work function W_{eff} (work function W). The gray dashed lines show the scale $\langle w \rangle \propto F_1^{2n}$.

emission current increases when considering the image-charge effect. A larger dc field, F_0, increases the emission current more significantly [$F_0 = 1$ V/nm in Figs. 9(a) and 9(b) vs $F_0 = 5$ V/nm in 9(c) and 9(d)], since a smaller effective barrier, W_{eff}, is created. As F_2 increases, the difference between the emission current $\langle w \rangle$ with W_{eff} and with W becomes smaller. The increase of the emission current due to the inclusion of the image effect is relatively insensitive to the phase delay, θ, of the two-color lasers. It is also important to note that, with the inclusion of W_{eff}, the slope of $\langle w \rangle$ decreases, as observed from the value of n in the scale $\langle w \rangle \propto F_1^{2n}$, which indicates that the number of photons involved in the dominant emission process decreases because of the deduction of the potential barrier near the metal surface.

IV. APPLICATION TO TIME-RESOLVED PHOTOELECTRON SPECTROSCOPY

Photoelectron spectroscopy is one of the most popular techniques to study the composition and electronic states of solid surfaces by analyzing the energy spectra [38,39]. Particularly, time-resolved photoemission spectroscopy enables the measurement of short lifetimes of the intermediate states, such as the image-potential states on metal surface, via control of the time delay between the pump and probe photons [40–42]. Here, we demonstrate the application of our quantum analytical model to describe the dynamics of different n-photon excited states in time and energy. As shown in Fig. 10(a), our 1D model is able to provide excellent fitting to the measured photoelectron spectra in Ref. [9] for the tungsten nanotip, by using a dc field of $F_0 = 0.01$ V/nm and an effective work function of $W_{\mathrm{eff}} = 3.85$ eV. Furthermore, the current modulation profile (both magnitude and shape) obtained from our 1D model [29] agrees very well with the experimentally observed sinusoidal variation with a period of 2π for the relative phase delay θ, as shown in Fig. 10(b).

Notably, other models, including the simple tunneling rate model and 1D time-dependent density functional theory, fail to describe the experimental results of the sinusoidal profile (cf. Supplemental Material of [9]).

The photoelectron energy spectra from the tungsten nanotip under various dc fields are shown in Figs. 10(c) and 10(d), for $\theta = 0$ and $\theta = \pi$, respectively. In the calculation, for each dc field, the effective work function, W_{eff}, is approximated by determining the peak value in the surface barrier profile under dc bias [43, 44], $\Phi_{\mathrm{dc}}(x) = W - eF_0 d\ln[(2x + r)/r]/\ln[(2d/r) + 1] - C_s^2 r/2e(x^2 - r^2)$, where the second term is the axial potential profile near a parabolic tip with a radius of curvature r with d being a constant [$= 83$ nm to fit the spectra in Fig. 10(a)] [44], and the third term is the image-charge potential of a spherical surface, with $C_s = \sqrt{e^3/4\pi\epsilon_0} = 1.199985$ eV(V/nm)$^{-1/2}$ as the Schottky constant [43]. It is important to note that the photoelectron spectra are very sensitive to the applied dc field, F_0, as shown in Figs. 10(c) and 10(d). The shift of the dominant emission process to a smaller n with larger dc field, F_0, agrees with our discussions above. More importantly, the emission current density is increased by more than three orders of magnitude as F_0 is gradually increased from 0.01 to 0.09 V/nm; this could strongly facilitate the experimental detection of photoemission.

When the relative time delay θ changes from $-\pi$ to π, the variations of the photoelectron energy spectra during one period for $F_0 = 0.01$ and 0.09 V/nm are shown in Figs. 10(e) and 10(f), respectively. To clearly observe the dynamics of different excited states in time, Figs. 10(g) and 10(h) show the projection of the energy spectra in Figs. 10(e) and 10(f), respectively, on the $\theta - \langle w_n \rangle$ plane. When the dc field is small, with $F_0 = 0.01$ V/nm [see Fig. 10(g)], all the n-photon orders of the spectra are modulated in the same way as a function of the relative phase delay, θ, in agreement with the results in Ref. [9]. The rising tendency of the points along the phase difference, θ,
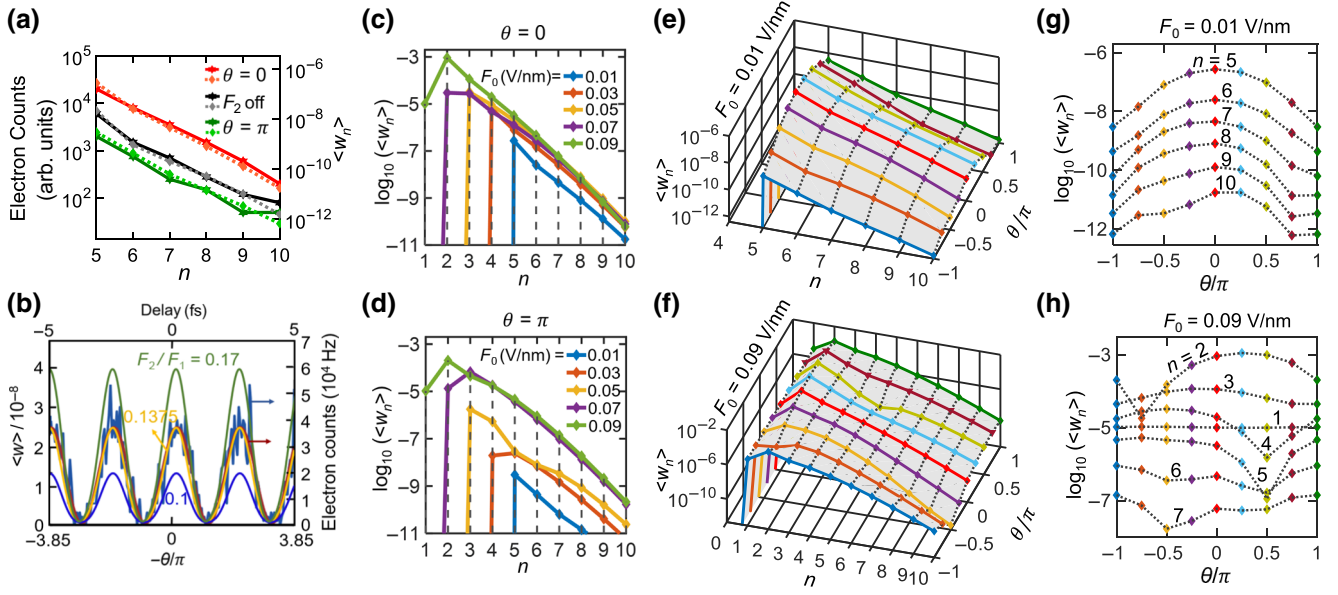
FIG. 10.　Time-resolved photoelectron energy spectra for the tungsten nanotip. (a) Comparison between the experimentally measured electron counts from Fig. 3 in Ref. [9] (see solid lines) and fitting results $\langle w_n \rangle$ (see dotted lines). (b) Normalized total time-averaged emission current density, $\langle w \rangle$, as a function of the phase difference between the two-color lasers, θ, for different F_2/F_1, with fixed $F_1 = 1.6$ V/nm. Blue and red lines denote the experimentally observed emission electron current and the sine fit from Fig. 2(b) in Ref. [9], respectively. (c),(d) Energy spectra for various dc fields, F_0, when (c) $\theta = 0$, and (d) $\theta = \pi$. (e),(f) Photoelectron spectra at different phase delays, θ, for the dc fields (e) $F_0 = 0.01$ V/nm and (f) $F_0 = 0.09$ V/nm. (g),(h) Projection of the spectra in (e),(f) on the $\theta - \langle w_n \rangle$ plane, respectively. Except for (b), the fundamental laser (1560 nm) field $F_1 = 1.8$ V/nm and the second-harmonic laser field $F_2 = 0.3$ V/nm (experimental laser parameters in Ref. [9]).

from $-\pi$ to 0 indicates the population of the n-photon excited intermediate states induced by lasers, while the decreasing signal from 0 to π implies the decay of the excited states. When F_0 is increased to 0.09 V/nm [see Fig. 10(h)], it is interesting to find that, due to the effect of the dc field, various n-photon excited states behave differently with respect to time delay θ. For instance, the one-photon tunneling state is almost invariable as θ changes from $-\pi$ to π, but the two-photon state decreases significantly at $\theta = -3\pi/4$. In addition, for a small dc field, the value of n for the dominant excitation state remains unchanged over the relative phase delay θ [Fig. 10(g)], which means that the energy of the n-photon excited

intermediate state is independent of the time delay [40]. However, when the dc field is larger, n for the dominant excitation state changes with the relative phase delay θ [Fig. 10(h)].

For electron emitters under a dc bias, it is important to prevent breakdown and premature failure of the emitter tips. Table I lists the local dc fields (after field enhancement) of sharp tips achieved in experiments before breakdown for eight materials. It is known that nanostructures survive large fields better for short pulse durations. As mentioned earlier, a local dc field of up to 10 V/nm at sharp tips may be realized in experiments via a laboratory-scale setup based on a pulsed capacitor discharge [2,36] or powerful THz pulses [45].

TABLE I.　List of achieved local dc fields (after field enhancement) of sharp tips before breakdown for eight materials.

	Achieved local dc field (V/nm)
Au	8.8 [2]
W	9.64 [36]
Cu	10.35 [36]
Mo	8.09 [36]
Pt/Ir	16 [45]
Carbon fiber	10.7 [46]
Carbon nanotube (CNT)	14 [47]
CNT fiber	13.1 [48–50]

V. CONCLUSION

In summary, we construct an exact analytical solution for ultrafast electron emission from a dc-biased metal surface due to two-color laser fields, by solving the time-dependent Schrödinger equation. The analytical model is valid for arbitrary harmonic orders, laser intensities, phase differences between two lasers, and metal work function and Fermi level. Our calculations reveal various emission processes, including photoinduced over-barrier emission and tunneling emission, for different dc and laser

fields, and recover the trend in the experimentally measured energy spectra [5,7,9,20] and voltage- and power-dependent electron flux [2]. In addition to the properties of the two-color lasers (i.e., relative phase, intensity, and frequency), our model shows that the addition of a dc field to the metal surface can provide great tunability of the photoemission energy spectra and current modulation depth for two-color laser-induced photoemission. Furthermore, the dc bias can increase the emission current by orders of magnitude. This increase of the current emission is due to the combined effects of potential barrier narrowing and barrier lowering. The former opens up more emission channels for multiphoton emission; the latter is attributed to the image-charge effects (or Schottky effect). Both effects significantly enhance the overall current emission. Various combinations of laser parameters and the dc field could provide great flexibility for the coherent control of ultrafast electron emission. Our results suggest a practical way to maintain a strong current modulation, while increasing the total emission current by orders of magnitude in two-color laser-induced electron emission, by simply using a strong dc bias and a weak harmonic laser. This simple, but effective, knob of dc bias will provide flexible control of both emission current and emitted electron energy spectra. This work will enable applications that require both a high current level and strong current modulation, e.g., miniaturized particle accelerators, photoelectron microscopy, and ultrafast electron sources. Moreover, being verified against the experimentally measured time-resolved photoelectron energy spectra [9], the results from our model are expected to guide future experiments on time-resolved photoemission spectroscopy.

Future research includes a comparison of the analytical model and standard numerical solutions for two-color photoemission, which will provide further benchmarks for our analytical results. When one of the laser fields has a high photon energy and/or shorter pulse duration, our analytical model may be directly applied to model a pump-probe experiment, where effects such as photoemission from population-enhanced surface states, excitation of electronic band structures and surface states of cathode materials, and hot carriers can be explored. The effects of electron thermal redistribution inside the metal due to laser heating, and thus induced transient change of Fermi energy from two-color photoemission will be investigated in future research. The effects of defects or impurity will be studied by considering the energy-dependent electron supply function inside the material and work-function variations along the emission surface. The scattering effects between electrons in the finite laser penetration depth will also be examined and compared with the existing three-step model [51] and Fowler-Dubridge model [52]. The carrier-envelope-phase effects [6,20,53,54] on photoelectron emission based on our quantum mechanical model will be studied.

Ultimately, it is envisioned that a hybrid model can be built around our exact analytical solution for simulating electron emission in practical geometries, such as sharp metal tips or cathodes with surface roughness, where effects such as the electron emission angle and space charge can be incorporated. The time-dependent field distribution near the emitter may be first calculated using a Maxwell solver. Next, our exact model can be applied along the surface of the emitter to give the instantaneous emission current. The emitted electrons can then be loaded into a particle-in-cell pusher to account for the detailed space charge effects and electron dynamics. Once such a tool becomes available, it would find immense applications in various areas, such as solid-state physics, strong fields, ultrafast sciences, vacuum electronics, and accelerators and beams.

APPENDIX

Following Truscott [29,30,55], the time-dependent potential for $x \geq 0$ may be written as $\Phi(x,t) = V(x) - xf(t)$, with $V(x) = V_0 - eF_0 x$, and $f(t) = eF_1 \cos(\omega t) + eF_2 \cos(\beta\omega t + \theta)$. Thus, Eq. (2) can be transformed into the coordinate system ξ, t, where $\xi = x - q(t)$, the displacement is $q(t) = (1/m) \int^t p(t')dt'$, and $p(t) = \int^t f(t')dt'$, by assuming that $\psi(x,t) = \phi(\xi,t)\chi(x,t)$, with $\chi(x,t) = \exp\left[-iEt/\hbar + ixp(t)/\hbar - (i/2\hbar m)\int^t p^2(t')dt'\right]$, and E is a constant:

$$i\hbar\frac{\partial\phi(\xi,t)}{\partial t} = \left[-\frac{\hbar^2}{2m}\frac{\partial^2}{\partial\xi^2} + U(\xi,t) - E\right]\phi(\xi,t), \quad (A1)$$

with $U(\xi,t) = V_0 - eF_0[\xi + q(t)]$. By separation of variables, Eq. (A1) can be solved to give

$$\phi(\xi,t) = g(\xi)$$
$$\times \exp\left[\frac{e^2 F_0 F_1 \sin(\omega t)}{i\hbar m\omega^3} + \frac{e^2 F_0 F_2 \sin(\beta\omega t + \theta)}{i\hbar m\beta^3\omega^3}\right], \quad (A2)$$

where $g(\xi) = \text{Ai}(-\eta) - i\text{Bi}(-\eta)$ is the solution of the equation $-(\hbar^2/2m)\partial^2 g(\xi)/\partial\xi^2 + (V_0 - E - eF_0\xi)g(\xi) = 0$, where $\eta = (2emF_0/\hbar^2)^{1/3}[(E - V_0)/eF_0 + \xi]$ [32,33]. From $\psi(x,t) = \phi(\xi)\chi(x,t)$, we obtain Eq. (3), which is the exact solution to Eq. (2), upon using $E = \varepsilon + n\hbar\omega - e^2 F_1^2/4m\omega^2 - e^2 F_2^2/4m\beta^2\omega^2$.

[1] P. Hommelhoff, Y. Sortais, A. Aghajani-Talesh, and M. A. Kasevich, Field Emission Tip as a Nanometer Source of Free Electron Femtosecond Pulses, Phys. Rev. Lett. **96,** 077401 (2006).

[2] C. Ropers, D. R. Solli, C. P. Schulz, C. Lienau, and T. Elsaesser, Localized Multiphoton Emission of Femtosecond Electron Pulses from Metal Nanotips, Phys. Rev. Lett. **98,** 043907 (2007).

[3] R. Ganter, R. Bakker, C. Gough, S. C. Leemann, M. Paraliev, M. Pedrozzi, F. Le Pimpec, V. Schlott, L. Rivkin, and A. Wrulich, Laser-Photofield Emission from Needle Cathodes for Low-Emittance Electron Beams, Phys. Rev. Lett. **100,** 064801 (2008).

[4] R. Bormann, M. Gulde, A. Weismann, S. V. Yalunin, and C. Ropers, Tip-Enhanced Strong-Field Photoemission, Phys. Rev. Lett. **105,** 147601 (2010).

[5] M. Schenk, M. Krüger, and P. Hommelhoff, Strong-Field Above-Threshold Photoemission from Sharp Metal Tips, Phys. Rev. Lett. **105,** 257601 (2010).

[6] M. Krüger, M. Schenk, and P. Hommelhoff, Attosecond control of electrons emitted from a nanoscale metal tip, Nature **475,** 78 (2011).

[7] G. Herink, D. R. Solli, M. Gulde, and C. Ropers, Field-driven photoemission from nanostructures quenches the quiver motion, Nature **483,** 190 (2012).

[8] L. Wimmer, G. Herink, D. R. Solli, S. V. Yalunin, K. E. Echternkamp, and C. Ropers, Terahertz control of nanotip photoemission, Nat. Phys. **10,** 432 (2014).

[9] M. Förster, T. Paschen, M. Krüger, C. Lemell, G. Wachter, F. Libisch, T. Madlener, J. Burgdörfer, and P. Hommelhoff, Two-Color Coherent Control of Femtosecond Above-Threshold Photoemission from a Tungsten Nanotip, Phys. Rev. Lett. **117,** 217601 (2016).

[10] W. C.-W. Huang, M. Becker, J. Beck, and H. Batelaan, Two-color multiphoton emission from nanotips, New J. Phys. **19,** 023011 (2017).

[11] L. Seiffert, T. Paschen, P. Hommelhoff, and T. Fennel, High-order above-threshold photoemission from nanotips controlled with two-color laser fields, J. Phys. B: At., Mol. Opt. Phys. **51,** 134001 (2018).

[12] J. S. Kim, T. LaGrange, B. W. Reed, M. L. Taheri, M. R. Armstrong, W. E. King, N. D. Browning, and G. H. Campbell, Imaging of transient structures using nanosecond in situ TEM, Science **321,** 1472 (2008).

[13] A. H. Zewail, Four-dimensional electron microscopy, Science **328,** 187 (2010).

[14] T. L. Cocker, D. Peller, P. Yu, J. Repp, and R. Huber, Tracking the ultrafast motion of a single molecule by femtosecond orbital imaging, Nature **539,** 263 (2016).

[15] A. Feist, N. Bach, N. Rubiano da Silva, T. Danz, M. Möller, K. E. Priebe, T. Domröse, J. G. Gatzmann, S. Rost, J. Schauss, S. Strauch, R. Bormann, M. Sivis, S. Schäfer, and C. Ropers, Ultrafast transmission electron microscopy using a laser-driven field emitter: Femtosecond resolution with a high coherence electron beam, Ultramicroscopy **176,** 63 (2017).

[16] P. G. O'Shea and H. P. Freund, Free-electron lasers: status and applications, Science **292,** 1853 (2001).

[17] I. Grguraš, A. R. Maier, C. Behrens, T. Mazza, T. J. Kelly, P. Radcliffe, S. Düsterer, A. K. Kazansky, N. M. Kabachnik, T. Tschentscher, J. T. Costello, M. Meyer, M. C. Hoffmann, H. Schlarb, and A. L. Cavalieri, Ultrafast X-ray pulse characterization at free-electron lasers, Nat. Photonics **6,** 852 (2012).

[18] P. Hommelhoff, C. Kealhofer, and M. A. Kasevich, Ultrafast Electron Pulses from a Tungsten Tip Triggered by Low-Power Femtosecond Laser Pulses, Phys. Rev. Lett. **97,** 247402 (2006).

[19] G. Wachter, C. Lemell, and J. Burgdörfer, Electron rescattering at metal nanotips induced by ultrashort laser pulses, J. Phys.: Conf. Ser. **488,** 012005 (2014).

[20] B. Piglosiewicz, S. Schmidt, D. J. Park, J. Vogelsang, P. Groß, C. Manzoni, P. Farinello, G. Cerullo, and C. Lienau, Carrier-envelope phase effects on the strong-field photoemission of electrons from metallic nanostructures, Nat. Photonics **8,** 37 (2014).

[21] E. Forati, T. J. Dill, A. R. Tao, and D. Sievenpiper, Photoemission-based microelectronic devices, Nat. Commun. **7,** 13399 (2016).

[22] E. Forati and D. Sievenpiper, Electron emission by long and short wavelength lasers: Essentials for the design of plasmonic photocathodes, J. Appl. Phys. **124,** 083101 (2018).

[23] P. Zhang, Á Valfells, L. K. Ang, J. W. Luginsland, and Y. Y. Lau, 100 years of the physics of diodes, Appl. Phys. Rev. **4,** 011304 (2017).

[24] P. Zhang and Y. Y. Lau, Ultrafast and nanoscale diodes, J. Plasma Phys. **82,** 595820505 (2016).

[25] J. Lin, P. Y. Wong, P. Yang, Y. Y. Lau, W. Tang, and P. Zhang, Electric field distribution and current emission in a miniaturized geometrical diode, J. Appl. Phys. **121,** 244301 (2017).

[26] H. Yanagisawa, C. Hafner, P. Doná, M. Klöckner, D. Leuenberger, T. Greber, M. Hengsberger, and J. Osterwalder, Optical Control of Field-Emission Sites by Femtosecond Laser Pulses, Phys. Rev. Lett. **103,** 257603 (2009).

[27] H. Yanagisawa, C. Hafner, P. Doná, M. Klöckner, D. Leuenberger, T. Greber, J. Osterwalder, and M. Hengsberger, Laser-Induced Field Emission from a Tungsten Tip: Optical Control of Emission Sites and the Emission Process, Phys. Rev. B **81,** 115429 (2010).

[28] S. V. Yalunin, M. Gulde, and C. Ropers, Strong-field photoemission from surfaces: Theoretical approaches, Phys. Rev. B **84,** 195426 (2011).

[29] Y. Luo and P. Zhang, Ultrafast strong-field photoelectron emission due to two-color laser fields, Phys. Rev. B **98,** 165442 (2018); Erratum, ibid, **99,** 169907 (2019).

[30] P. Zhang and Y. Y. Lau, Ultrafast strong-field photoelectron emission from biased metal surfaces: exact solution to time-dependent Schrödinger Equation, Sci. Rep. **6,** 19894 (2016).

[31] T. Paschen, M. Förster, M. Krüger, C. Lemell, G. Wachter, F. Libisch, T. Madlener, J. Burgdörfer, and P. Hommelhoff, High visibility in two-color above-threshold photoemission from tungsten nanotips in a coherent control scheme, J. Mod. Opt. **64,** 1054 (2017).

[32] R. H. Fowler and L. Nordheim, Electron emission in intense electric fields, Proc. R. Soc. London, Ser. A **119,** 173 (1928).

[33] J. W. Gadzuk and E. W. Plummer, Field emission energy distribution (FEED), Rev. Mod. Phys. **45,** 487 (1973).

[34] P. Zhang, Scaling for quantum tunneling current in nano- and subnano-scale plasmonic junctions, Sci. Rep. **5,** 9826 (2015).

[35] H. B. Michaelson, The work function of the elements and its periodicity, J. Appl. Phys. **48,** 4729 (1977).

[36] M. Kildemo, S. Calatroni, and M. Taborelli, Breakdown and field emission conditioning of Cu, Mo, and W, Phys. Rev. Spec. Top. Accel. Beams **7,** 092003 (2004).

[37] L. V. Keldysh, Ionization in the field of a strong electromagnetic wave, Sov. Phys. JETP **20,** 1307 (1964).

[38] R. Haight, Electron dynamics at surfaces, Surf. Sci. Rep. **21,** 275 (1995).

[39] F. Reinert and S. Hüfner, Photoemission spectroscopy— from early days to recent applications, New J. Phys. **7,** 97 (2005).

[40] R. W. Schoenlein, J. G. Fujimoto, G. L. Eesley, and T. W. Capehart, Femtosecond relaxation dynamics of image-potential states, Phys. Rev. B **43,** 4688 (1991).

[41] M. Weinelt, Time-resolved two-photon photoemission from metal surfaces, J. Phys. Condens. Matter **14,** R1099 (2002).

[42] D. Friedrich, P. Sippel, O. Supplie, T. Hannappel, and R. Eichberger, Two-photon photoemission spectroscopy for studying energetics and electron dynamics at semiconductor interfaces, Phys. Status Solidi A **216,** 1800738 (2019).

[43] J. T. Holgate and M. Coppins, Field-Induced and Thermal Electron Currents from Earthed Spherical Emitters, Phys. Rev. Appl. **7,** 044019 (2017).

[44] Y. Fu, J. Krek, P. Zhang, and J. P. Verboncoeur, Evaluating microgap breakdown mode transition with electric field non-uniformity, Plasma Sources Sci. Technol. **27,** 095014 (2018).

[45] K. Yoshioka, I. Katayama, Y. Minami, M. Kitajima, S. Yoshida, H. Shigekawa, and J. Takeda, Real-space coherent manipulation of electrons in a single tunnel junction by single-cycle terahertz electric fields, Nat. Photonics **10,** 762 (2016).

[46] W. Tang, D. Shiffler, K. Golby, M. LaCour, and T. Knowles, Field enhancement for fiber emitters in linear and rectangular arrays, J. Vac. Sci. Technol. B **32,** 052202 (2014).

[47] S. H. Jo, J. Y. Huang, S. Chen, G. Y. Xiong, D. Z. Wang, and Z. F. Ren, Field emission of carbon nanotubes grown on carbon cloth, J. Vac. Sci. Technol. B **23,** 2363 (2005).

[48] P. Zhang, S. B. Fairchild, T. C. Back, and Y. Luo, Field emission from carbon nanotube fibers in varying anode-cathode gap with the consideration of contact resistance, AIP Adv. **7,** 125203 (2017).

[49] P. Zhang, J. Park, S. B. Fairchild, N. P. Lockwood, Y. Y. Lau, J. Ferguson, and T. Back, Temperature comparison of looped and vertical carbon nanotube fibers during field emission, Appl. Sci. **8,** 1175 (2018).

[50] S. B. Fairchild, P. Zhang, J. Park, T. C. Back, D. Marincel, Z. Huang, and M. Pasquali, Carbon nanotube fiber field emission array cathodes, IEEE Trans. Plasma Sci. **47,** 2032 (2019).

[51] D. H. Dowell and J. F. Schmerge, Quantum efficiency and thermal emittance of metal photocathodes, Phys. Rev. Spec. Top. Accel. Beams **12,** 074201 (2009).

[52] J. H. Bechtel, W. Lee Smith, and N. Bloembergen, Two-photon photoemission from metals induced by picosecond laser pulses, Phys. Rev. B **15,** 4557 (1977).

[53] C. Lemell, X.-M. Tong, F. Krausz, and J. Burgdörfer, Electron Emission from Metal Surfaces by Ultrashort Pulses: Determination of the Carrier-Envelope Phase, Phys. Rev. Lett. **90,** 076403 (2003).

[54] A. Apolonski, P. Dombi, G. G. Paulus, M. Kakehata, R. Holzwarth, T. Udem, C. Lemell, K. Torizuka, J. Burgdörfer, T. W. Hänsch, and F. Krausz, Observation of Light-Phase-Sensitive Photoemission from a Metal, Phys. Rev. Lett. **92,** 073902 (2004).

[55] W. S. Truscott, Wave Functions in the Presence of a Time-Dependent Field: Exact Solutions and Their Application to Tunneling, Phys. Rev. Lett. **70,** 1900 (1993).